



Article

Analysis of Seasonal and Long-Term Variations in the Surface and Vertical Structures of the Lofoten Vortex

Yu Liu ^{1,2} , Jing Meng ¹, Jianhui Wang ³, Guoqing Han ^{1,*}, Xiayan Lin ¹, Junming Chen ^{4,5} and Qiyan Ji ¹

¹ Marine Science and Technology College, Zhejiang Ocean University, Zhoushan 316000, China; liuyuhk@zjou.edu.cn (Y.L.); mengjing@zjou.edu.cn (J.M.); linxiayan@zjou.edu.cn (X.L.); jiqiyan@zjou.edu.cn (Q.J.)

² Southern Marine Science and Engineering Guangdong Laboratory (Zhuhai), Zhuhai 519000, China

³ Fourth Institute of Oceanography, Ministry of Natural Resources, Beihai 536007, China; wangjianhui@4io.org.cn

⁴ State Key Laboratory of Severe Weather, Chinese Academy of Meteorological Sciences, Beijing 100081, China; chenjm@cma.gov.cn

⁵ China Meteorological Administration Xiong'an Atmospheric Boundary Layer Key Laboratory, Xiong'an New Area, Baoding 071799, China

* Correspondence: hanguoqing@zjou.edu.cn

Abstract: The Lofoten Vortex (LV) is a quasi-permanent anticyclonic eddy with the characteristic of periodic regeneration in the Lofoten Basin (LB), which is one of the major areas of deep vertical mixing in the Nordic Sea. Our analysis of the LV contributes to our understanding of the variations in convective mixing in the LB. Based on drifter data and satellite altimeter data, the climatological results show that the LV has the sea surface characteristics of relative stability in terms of its spatial position and significant seasonal variations in its physical characteristics. Combined with the temperature and salinity data of Argo profiles, the vertical structures of the LV are presented here in terms of their spatial distribution and monthly variations. The wavelet analysis of the satellite sea surface temperature (SST) data shows that the period of SST anomaly (SSTA) in the LV sea area is 8–16 years. In the stage marked by a decreasing (increasing) trend of SSTA, the vertical mixing is strengthened (weakened). Current vertical mixing is clearly revealed by the Argo profiles, and the SSTA shows a significant impact of cooling. However, against a background of warming and freshening, this vertical mixing will be greatly weakened in the next increasing trending stage of the SSTA.

Keywords: the Lofoten Vortex; Argo profiles; sea surface temperature; vertical mixing



Citation: Liu, Y.; Meng, J.; Wang, J.; Han, G.; Lin, X.; Chen, J.; Ji, Q.

Analysis of Seasonal and Long-Term Variations in the Surface and Vertical Structures of the Lofoten Vortex.

Remote Sens. **2023**, *15*, 1903.

<https://doi.org/10.3390/rs15071903>

Academic Editor: Mark Bourassa

Received: 9 February 2023

Revised: 30 March 2023

Accepted: 31 March 2023

Published: 2 April 2023



Copyright: © 2023 by the authors. Licensee MDPI, Basel, Switzerland. This article is an open access article distributed under the terms and conditions of the Creative Commons Attribution (CC BY) license (<https://creativecommons.org/licenses/by/4.0/>).

1. Introduction

Located at approximately 70°N in the eastern Nordic Seas, the Lofoten Basin (LB) is surrounded by the Norwegian Atlantic Slope Current (NwASC) and the Norwegian Atlantic Front Current (NwAFC) (shown in Figure 1a). The LB is filled with warm and salty Atlantic water, which occupies the upper 800 m [1–3] and serves as the primary heat reservoir in the Norwegian Sea [4]. However, the LB undergoes significant heat loss, rendering it the Nordic Seas' largest heat loss site [5]. Prior to reaching the Barents Sea and the Fram Strait [6], the Atlantic water has already lost approximately half of its heat content (250 TW) due to strong sea–air interactions and the lateral mixing of vortices. Additionally, the LB is a significant area of deep vertical mixing in the Nordic Seas [7], contributing to the formation of the North Atlantic Deep Water (NADW) [8–10] and playing a crucial role in maintaining Atlantic meridional overturning circulation [11]. Consequently, the LB has become one of the focal study areas in the pan-Arctic region [12].

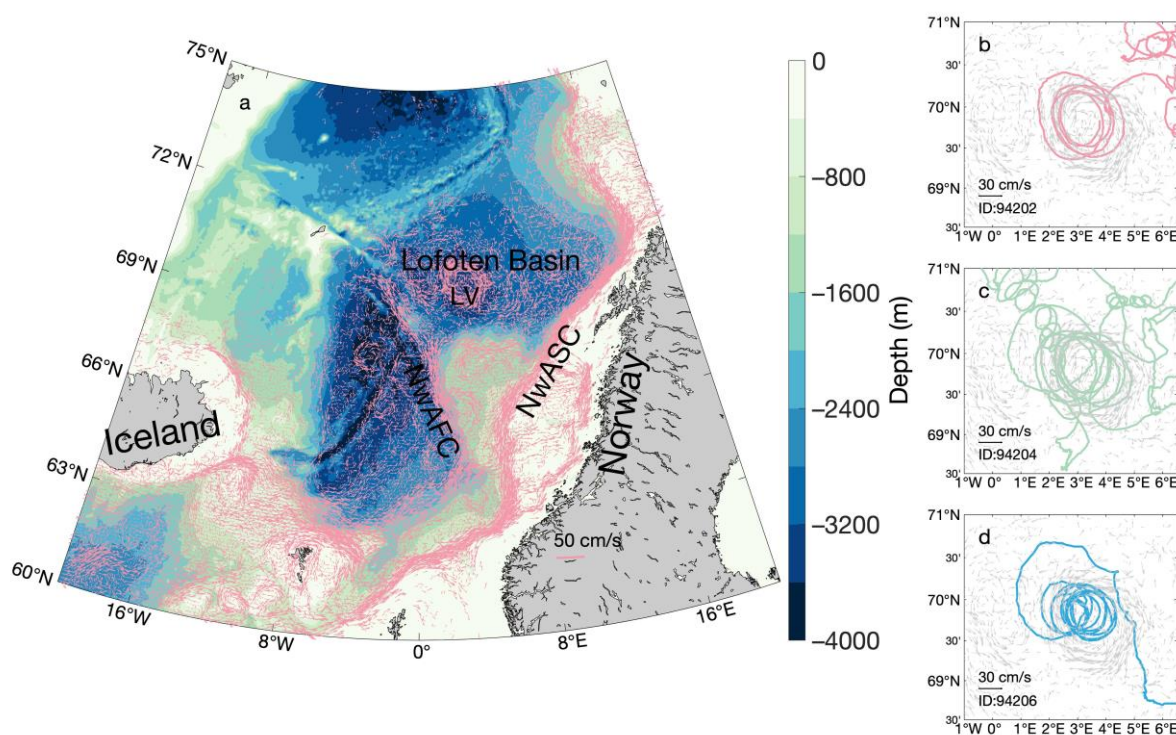


Figure 1. Map of the Nordic Seas, together with the climatological currents derived from the GDP data. (a) Climatological Lofoten Vortex (CLV), Norwegian Atlantic Slope Current, and Norwegian Atlantic Front Current. Loop trajectories of drifters captured by the LV: (b) ID 94202, (c) ID 94202, and (d) ID 94206.

Mesoscale eddies are active in the LB [13,14]. This activity is supported by the local maximum of eddy kinetic energy in the Nordic Seas. Some eddies are separated from the NwASC [15–18]. Barotropic energy conversion rates reveal the energy transfer from the slope current to the eddies during winter [13]. These eddies play a significant role in extracting warm and salty water from the NwASC and redistributing it throughout the LB. Some eddies are generated from various frontal zones, such as the NwAFC [14]. The mesoscale eddies strongly affect the thermohaline structure of the LB [19] and regulate the transportation of heat and salt by the Atlantic water to the polar region [20–22].

One of the eddies present in the LB is called the Lofoten Vortex (LV), which is easily distinguishable from the climatological flow field (Figure 1a) and the periodic loop trajectories of the drifting buoys (Figure 1b–d). The LV is an anticyclonic eddy located at approximately 70° N and 4° E in a region of the sea with a depression in terms of its topography. Its average radius is around 37 km, and it has an average tangential velocity of approximately 30 cm s^{-1} [13]. In the vertical direction, the LV can be identified by its positive temperature and salinity anomalies found between the depths of 400 and 2000 m [23–27], with the strongest signal at approximately 800 m [23,28].

Seasonal variation in the LV is evident, exhibiting higher activity during the winter and spring months. Previous investigations based on marine surveys between 1985 and 1991 have shown that the temperature and salt anomalies of the LV become more prominent during these seasons [24]. This observation has been further confirmed by data obtained from drifting buoy trajectory and satellite altimetry [29,30]. During winter, the LV radius contracts and its rotation speed increases, whereas during summer, the radius expands and the rotation speed decreases. The LV is surrounded by long-lived cyclonic eddies (CEs), which serve as a protective barrier [14]. Due to its interaction with ambient cyclonic eddies, in general, the LV follows an anticyclonic trajectory [17].

The LV is considered as a periodic rejuvenation or quasi-permanent eddy [14,24,25,31]. The quasi-permanence of the LV can be attributed to two dynamic mechanisms. One

mechanism involves winter convection, whereby strong convective mixing during winter strengthens the LV and enhances its abnormal density. The other mechanism involves merging with other anticyclonic eddies (ACEs) [13,17,32]. These ACEs are shed from the intensified NwASC, and the basin's depression attracts them toward the basin center. Repeated merging events enhance and stabilize the LV [17,33], resulting in a new, axisymmetric, double-core vortex through vertical alignment [32]. A similar double-core structure was also observed by Belkin et al. [34]. Wintertime convection primarily serves to vertically homogenize and densify the vortex, rather than intensifying it [32]. The combination of these two mechanisms explains the strengthening of the LV.

The LV's relatively stable spatial position and periodic regeneration make it an ideal eddy for studying theoretical concepts about eddies. Although many studies have focused on eddy-induced heat and salt transport, an investigation of the LV's stable spatial variations could provide insight into dynamic variations in vertical mixing and eddy merging. As the vertical mixing of the LV may be a potential indicator of the strengthening of, and periodic variations in, the NADW, it is worth studying.

In this paper, we use surface satellite data and vertical Argo profile data to study the surface and vertical structures of the LV, establish a relationship between SST and vertical mixing, and then determine the long-term variations in the surface and vertical structures of the LV.

2. Data

2.1. Drifter Data

The drifter data were obtained from the Global Drifter Program (GDP, <https://www.aoml.noaa.gov/phod/gdp/index.php> accessed on 15 September 2022). The data files record the position, time, and locations (latitude and longitude) of the drifters, sea surface temperatures (SSTs), and current velocity components every 6 h.

We extracted the records of 989 drifters in the Nordic Seas from 11 April 1991 to 18 February 2022 (60°N–80°N, 20°W–20°E) and 437 drifters in the Norwegian Sea from 05-06-1991 to 18 February 2022 (65°N–72°N, 2°W–12°E).

The climatological flow field was averaged within $0.1^\circ \times 0.1^\circ$ bins using the drifter velocity data from 11 April 1991 to 18 February 2022. We only chose bins for which the data record number was larger than 15. We obtained information on the center and location of the CLV and its basic circulation from the climatological flow field. We also determined the loop trajectories from the drifter data [35].

2.2. Sea Surface Height (SSH) Data

The SSH data we used concerned the absolute dynamic topography (ADT) from AVISO. The ADT is a daily global level-4 product, which covers the period from September 1981 to the present and has a $0.25^\circ \times 0.25^\circ$ horizontal resolution. The ADT and its derived geostrophic current data were obtained from the Copernicus Marine Environment Monitoring Service (CMEMS, <http://marine.copernicus.eu/> accessed on 22 September 2022). Our study area, the LB, is at a high latitude at approximately 70°N. Compared with the zonal grid space, the meridional grid space is lower. To properly present the flow field, we interpolated the data into $0.125^\circ \times 0.125^\circ$ horizontal grid data. The final data we used covered approximately 5 and 15 km in the longitude and latitude directions, respectively. To display the images properly, we plotted the vector field in every two grids in the zonal direction to render it generally uniformed with the meridional direction. It should be noted that the interpolation did not affect our results.

2.3. SST Data

The SST data we analyzed were based on observations from multiple infrared satellite sensors, including a series of Advanced Very High Resolution Radiometers, a series of Along-Track Scanning Radiometers, and a Sea and Land Surface Temperature Radiometer. The SST data are daily global level-4 products, which cover the period from September 1981

to December 2021 and have a $0.05^\circ \times 0.05^\circ$ horizontal resolution. The SST data were also download from CMEMS (<https://marine.copernicus.eu/> accessed on 22 November 2022).

2.4. Argo Buoy Data

The vertical temperature and salinity profile data were obtained from Argo buoy observations. The daily products were downloaded from <ftp://ftp.ifremer.fr/ifremer/argo/geo>, accessed on 25 September 2022. The Argo profile files provided quality control flags. We only chose data of “good level” quality. It should be noted that absolute salinity is the appropriate representation of salinity for use in dynamical physical oceanography [36]. Here, we used the potential temperature and the practical salinity. All profile data were interpolated into standard vertical grids with a 2 m resolution, ranging from 20 m to 2000 m in depth.

3. Methods

3.1. Composite Analysis of the Vertical Structure of LV

To investigate the vertical structure of the LV from an observational point of view, we sorted and classified all the available Argo profiles of areas within and around the LV from Jan. 2002 to Mar. 2022.

Based on the averaged flow field from the velocities measured by the drifters and the geostrophic currents derived from the ADT, the center of the climatological LV (CLV) was identified as 69.8°N , 3.3°E . The spatial distribution of the Argo buoys around the CCLV is shown in Figure 2a. From a circle with a radius of 60 km, 632 “good level” Argo profiles (blue dots) were selected. From a ring with a radius of 60–120 km, 1188 Argo profiles (pink dots) were chosen.

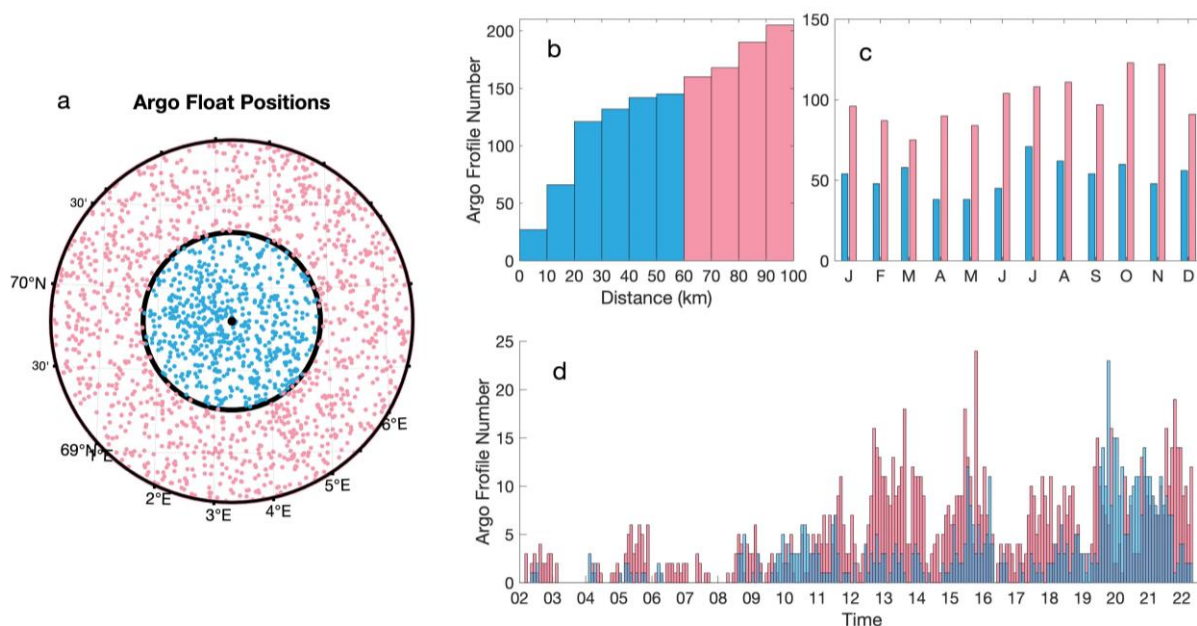


Figure 2. Spatial–temporal distribution of the Argo profiles of areas around the CLV from Jan. 2002 to Mar. 2022. (a) Position of Argo floats. (b) Argo profile numbers with increasing distance from the CCLV. (c) Seasonal quantity distribution and (d) monthly quantity distribution of the Argo profiles from Jan. 2002 to Mar. 2022. The blue dots or bins are the Argo positions or numbers within the CLV with a radius of 60 km, and the pink dots or bins are the Argo positions or numbers within a cyclic ring with a radius of 60–120 km.

To investigate the spatial structure of the CLV, the Argo profiles were sorted according to the geographical distribution of the ring with a radius difference of 10 km around the CCLV. The Argo profile numbers within the ring are shown in Figure 2b. These

classified profiles are used to analyze the climatological vertical characteristics of the CLV in Section 4.2.

To investigate the temporal variation in the vertical structure, the Argo profiles were also sorted by month. The climatological monthly quantity and the month-to-month quantity of the Argo profiles are shown in Figure 2c,d. The blue bins are the monthly numbers of Argo buoys in the CLV within a radius of 60 km, and the pink bins are the monthly numbers in a ring within a radius of 60–120 km. These classified profiles are used to analyze the seasonal variations in the CLV in Section 4.3 and the long-term trend change in Section 4.4.

3.2. Wavelet Analysis of the SST Time Series of LV

Wavelet analysis is a common tool for analyzing a time series [37]. By decomposing a time series into time–frequency space, we can determine the dominant modes and their variations over time. We used wavelet analysis to analyze the LV SST time series [38]. Compared with the Paul wavelet and the Morlet wavelet, the wavelet basis function we used was the DOG wavelet. This wave is modulated by the m -order derivative of a Gaussian envelope, as follows:

$$\psi_0(\eta) = \frac{(-1)^{m+1}}{\sqrt{\Gamma\left(m + \frac{1}{2}\right)}} \frac{d^m}{d\eta^m} \left(e^{-\eta^2/2} \right)$$

where $\eta = t/s$, t is time, and s is the wavelet scale. We chose $m = 6$.

The MATLAB code, including the statistical significance tests, can be downloaded from <https://paos.colorado.edu/research/wavelets/wavelet1.html> accessed on 26 November 2022.

4. Results

4.1. Climatological Surface Characteristics

Theoretically, eddy signals should be abstracted from disturbed velocity fields by removing the background (time-averaged) current from the original flow current fields. The LV is a quasi-permanent ACE. It is relatively spatially stable. Removing the mean background velocity will eliminate the LV signals. It is more reasonable to use the ADT and its derived geostrophic velocity data to present the LV. Here, the ADT data from 1 January 1993 to 9 February 2022 are averaged, and the spatial graphics of the physical characteristic parameters of the CLV are shown in Figure 3a–c. The CCLV was identified as being positioned at 69.8°N and 3.3°E. The coherent cores of the CLV are encircled by black boundary lines within a radius of 60 km.

The SSH difference (SSHD) in the LV is defined by the center zone and boundary zone (Figure 3b). The former is determined by the mean height in the black circle within a radius of 10 km. The latter is determined by the mean height in the dashed ring within a radius of 50–60 km. The climatological SSHD is approximately 12 cm. The outer tangential velocity is approximately 30 cm s⁻¹. The kinetic energy of the CLV is approximately 300 cm²s⁻². The vorticity of the CLV core is approximately -10^{-5} s⁻¹. There is a positive vorticity zone around the CLV with a local negative vorticity. Almost all the physical parameters demonstrate that the LV is a strong ACE.

The environmental variables of the LV show strong seasonal changes. The highest value of the ADT is reached in September, and the lowest value is observed in March. The strength of the LV is not determined by the ADT, but by the SSHD.

The climatological monthly variation in the SSHD features the maximum value in May and lower values from September to February in the following year. Correspondingly, the kinetic energy shows similar monthly variations. The variation in KE is similar to that seen in the previous results but concerns eddy kinetic energy [39]. The negative vorticity of the LV exhibits an opposite trend of variation, reaching the minimum value (strongest) in

May. These parameters are all averaged within a circle with a radius of 60 km. Although attracted by the depression terrain, the position of the LV is only partially stable. The LV moves and evolves through interactions with its surrounding CEs and merges with other ACEs. Not all physical variables of the LV have totally matched variations.

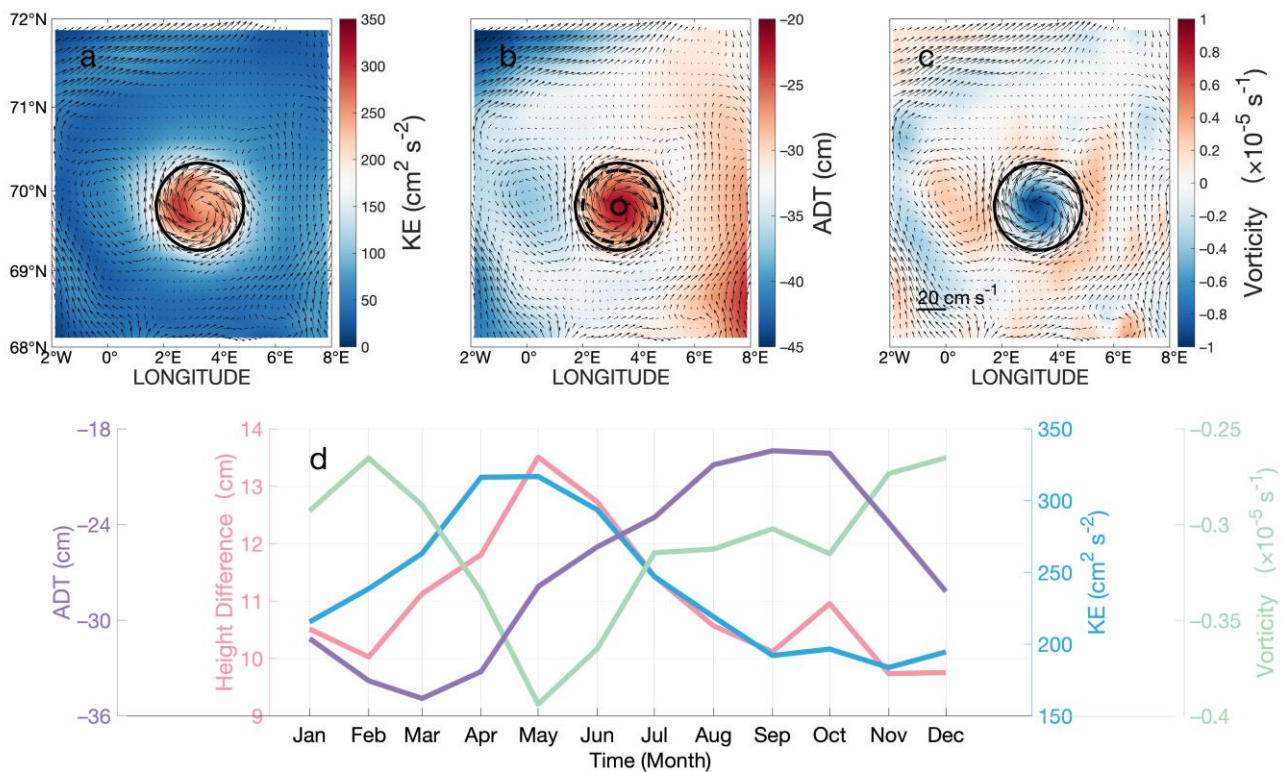


Figure 3. Spatial graphics of the climatological (a) kinetic energy, (b) ADT, and (c) vorticity of the CLV derived using daily AVISO sea-level data from 01-01-1993 to 09-02-2022. (d) Climatological monthly variation in the ADT, height difference, kinetic energy, and vorticity in the CLV. The height difference is the amplitude between the mean height within the black circle with a radius of 10 km and the mean height within the dashed ring with a radius of 50–60 km. The other parameters are averaged within the circle with a radius of 60 km.

4.2. Climatological Vertical Characteristics

Around the CCLV, 69.8°N and 3.3°E, the Argo profile number in the center zone is approximately 30, with a radius of 10 km, while it is approximately 60 in the first ring, with a radius of 10–20 km, and slightly increases from 120 to 200 in the successive rings, with a radius difference of 10 km, ranging from 20 km to 100 km (Figure 2b). These Argo profiles were selected between Jan. 2002 and Mar. 2022. We averaged these sorted profiles in rings to investigate the climatological vertical structure of the LV.

Generally, with an increasing depth from 20 m to 1500 m, the salinity range within the LV (0–60 km) ranges from 35.1 PSU to 34.9 PSU, the potential temperature ranges from 6 °C to −0.5 °C, and the potential density ranges from 27.6 kg m^{-3} to 28.05 kg m^{-3} (Figure 4). Traditionally, the AW is defined as having a water mass with $S > 35.0$ while it flows through the Norwegian seas toward Arctic [40]. The LV significantly deepens the AW within its sea area.

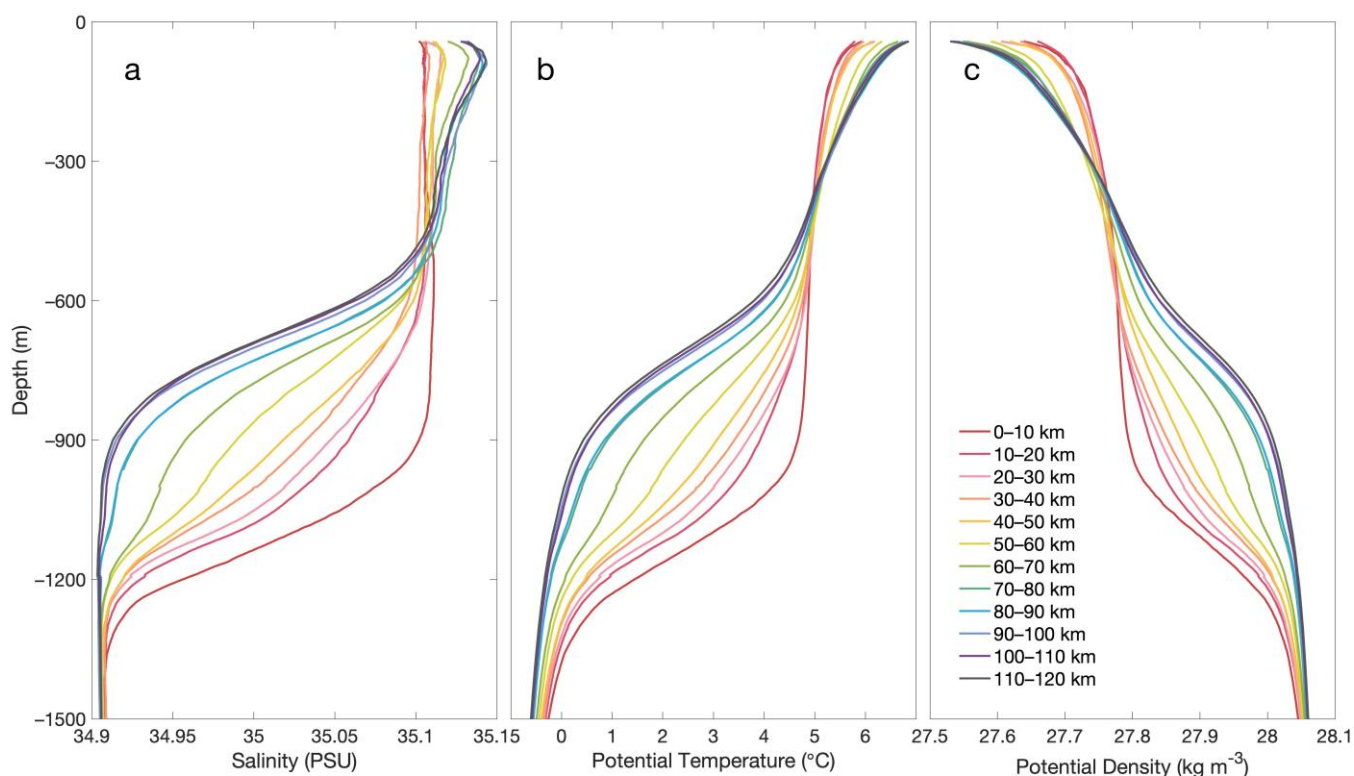


Figure 4. Climatological profiles derived from Argo: (a) practical salinity, (b) potential temperature, and (c) potential density profiles with increasing distance from the center of the CLV.

The vertical mixing characteristic is significant in the center zone, and its influence can reach a depth of 900–1000 m. This is the climatological result. Raj et al. [13] analyzed the Argo profiles of ACEs in the western LB and found that the penetration depth of the Atlantic water can reach 1200 m. Far from the center of the LV, the vertical mixing effect decreases. The vertical effective influence can reach a depth of approximately 400–500 m outside of the LV. In particular, in the center zone, with a radius of 10 km, the salinity maintains a value of 35.1 PSU, and the temperature is kept at 5 °C in the vertical direction at a depth of more than 900 m.

Correspondingly, the potential density is approximately 27.8 kg m⁻³ below the depth of 500 m and approximately 27.75 kg m⁻³ in the subsurface layer. These values are comparable with the overflow density values ($\sigma_{\theta} > 27.8 \text{ kg m}^{-3}$) of the Denmark Strait. These values show their potential importance for convection, deep-water formation, and global overturning circulation [10,41].

The ACE has the characteristics of horizontal convergence and vertical subsidence. Normally, horizontal convergence induces surface water within the eddy that is “warmer” and “saltier” than the surrounding water. Nevertheless, due to the strong vertical mixing effect, in the upper 500 m, the vortex shows the characteristic signals of being “colder” and “fresher” in the horizontal level. The LV is the “cold core” ACE in the upper layer. In the western LB, due to its being well mixed, the temperature inside the ACEs even tends to be slightly colder than that inside the CES in the upper ocean. However, the warmer waters can penetrate deeper into the ACEs, and their heat content is still greater than that of the CE [13].

While the core of the LV is concentrated at the depth of 500–1300 m, it presents anomaly signals of being “warmer” and “saltier.” At a depth of 900 m, the salinity anomaly is $\Delta S = 0.2 \text{ PSU}$, the potential temperature anomaly is $\Delta T = 5.5 \text{ °C}$, and the potential density anomaly is $\Delta \rho = -0.25 \text{ kg m}^{-3}$.

The surface merging evolution of the LV and one ACE (OAE) is shown by the vorticity and geostrophic current fields from 10 Jan. to 30 Jan. 2012 (Figure 5). Before 10 January

2012, these two ACEs had their own closed rotation flow fields. As the OAE gradually approached the LV, the two closed flow fields began to open up to one another. They were enveloped by a large rotating flow field. The flow field of the OAE stretched and deformed, and the vorticity field of the OAE gradually weakened. By 30 January 2012, the surface merging was completed. The LV was restored to a relatively standard shape.

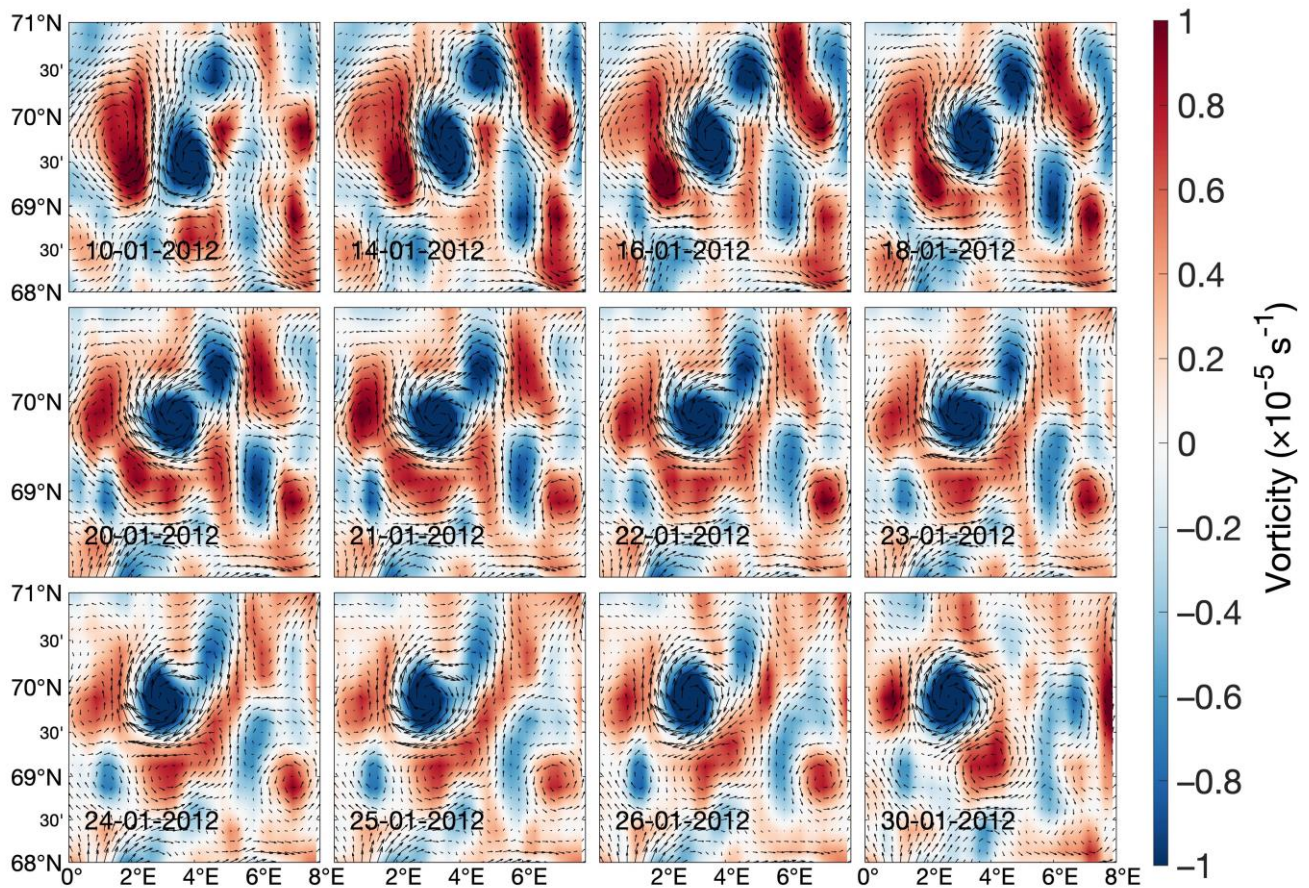


Figure 5. Merging evolution of the LV and OAE. The vorticity fields and geostrophic currents from 10-01-2012 to 30-01-2012 are shown.

In the Lagrangian view, it is important to know whether the intensity of the LV has regularity. The frequency rate of merging processes should depend on the attracted ACEs, which are partially born from the local area and partially shed from the NwASC. Additional statistics about the ACEs' generation, tracking, and merging are needed. Eddy detection, together with merging data, is necessary for the LB.

4.3. Seasonal Variations in Spatial Fields

Following the climatological monthly variations in Figure 3b, we present the spatial distributions of various physical parameters in two extreme months, May and September (Figure 6). With similar background values, the kinetic energy can reach higher than $300 \text{ cm}^2 \text{ s}^{-2}$ throughout the LV area in May but is approximately $200 \text{ cm}^2 \text{ s}^{-2}$ in Sep. The background ADT is approximately -40 – -35 m in May and approximately -30 – -25 m in Sep. Although the ADT is higher in Sep., the surface height difference throughout the LV area is higher in May. A strong shield with positive vorticity exists throughout the LV in May. The negative and positive vorticity inside and outside of the LV contrast significantly. The zero zones refer to the existing intensive ACEs.

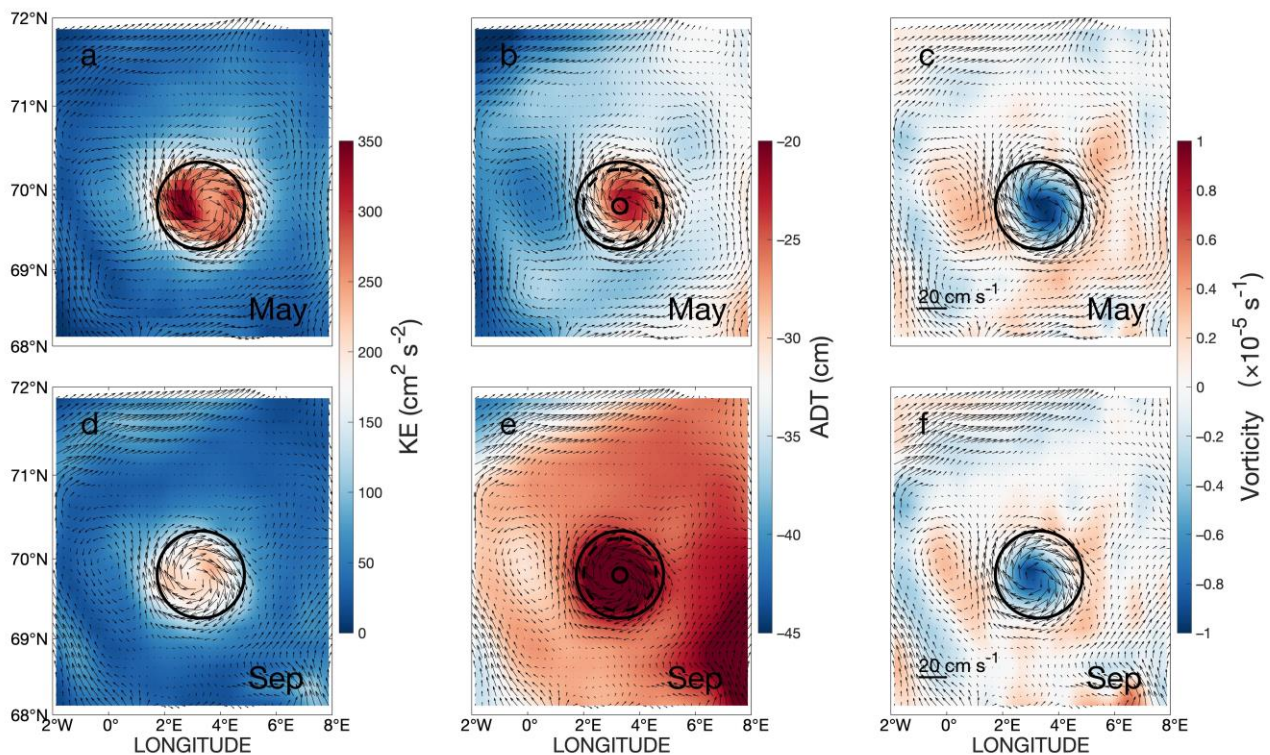


Figure 6. Seasonal comparison of the physical characteristics of the CLV. The upper panels show the climatological characteristics in May: (a) kinetic energy, (b) ADT, and (c) vorticity. The lower panels (d–f) are the climatological characteristics in September.

The center positions, coverages, and shapes of the LV are different in the daily comparisons (Figure 5). The state of the LV is affected by complex conditions, such as its own strength, movement through interactions with other CEs, and merging with other ACEs. Nonetheless, the spatial distributions show that the state conditions of the LV (the center positions, coverages, and shapes of the LV) are relatively stable, at least in the climatological months.

Based on the space-stable location, we first employed the Argo profiles to investigate the climatological monthly variations in the vertical structure. Being limited to the available profiles, we averaged all the climatological monthly Argo profiles. The climatological monthly number of Argo profiles is approximately 50 within the LV and approximately 100 within the outer-ring zone (Figure 2c). The climatological monthly salinity, potential temperature, and potential density profiles are presented in Figure 7. The solid profiles represent the LV water in the inner circle of the CLV within a radius of 60 km. The dashed profiles represent the background sea water in the outer ring of the CLV within a radius of 60–120 km. Here, we took the temperature as an example. In the upper 400 m, the background sea water temperature starts to warm up in May, reaches the highest value in September and October, and then cools down from November until the lowest value is reached in April. The sea water temperature within the LV has a similar seasonal variation but is cooler than the background sea water due to vertical mixing. At the LV core depth, of 600–1200 m, due to vertical mixing, the vertical penetration of the temperature and salinity inside the LV is deeper than that of the outside background water. The monthly vertical profiles of the background sea water have a slight difference. Meanwhile, the monthly vertical profiles of the area inside the LV show contradictory results. For instance, the surface CLV is stronger in May and weaker in September. A stronger LV will generate strong vertical mixing. The May climatological profiles for the vertical temperature of the CLV should be sharper than the September climatological profile. The position and quantity distributions of the Argo profiles are different in May and September. The limited

quantity of Argo profiles is still not enough for a comparison of the monthly climatological vertical profiles.

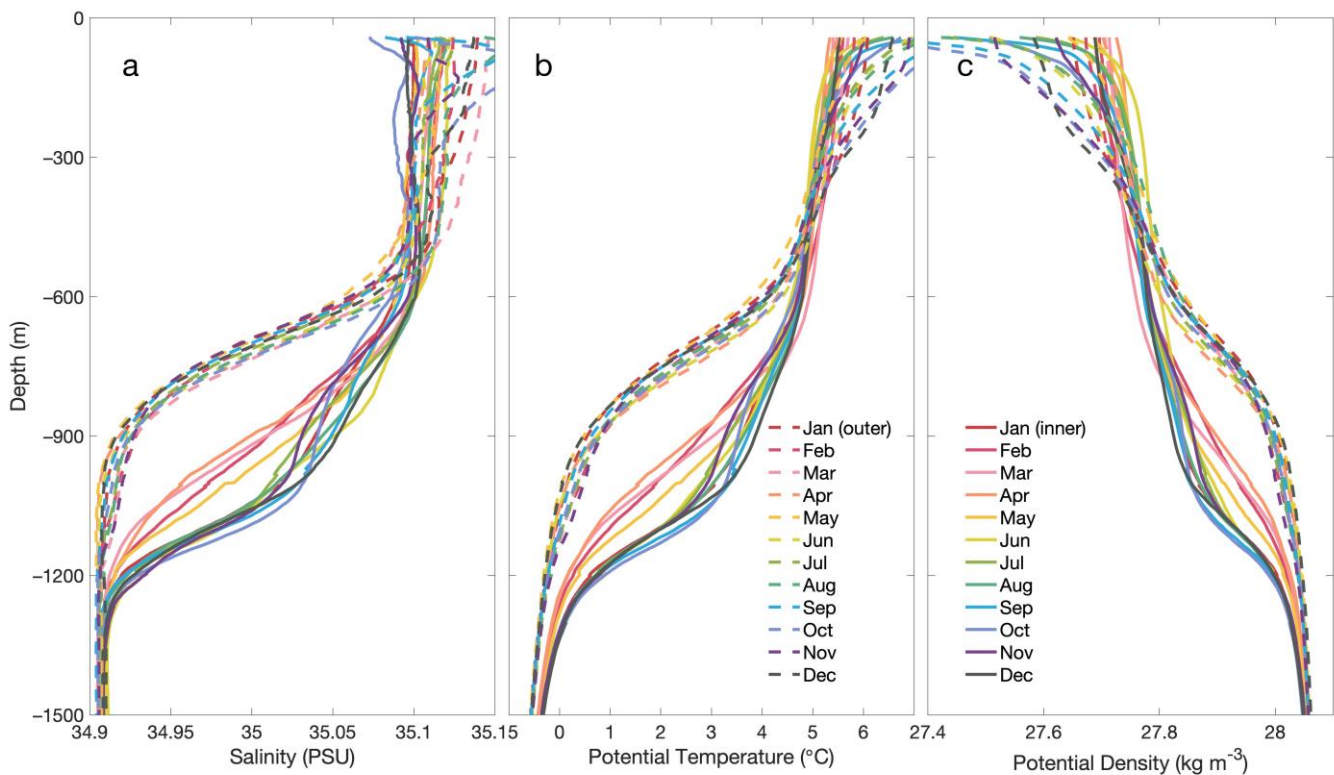


Figure 7. Climatological monthly (a) salinity, (b) potential temperature, and (c) potential density profiles. The solid profiles are in the inner circle of the CLV within a radius of 60 km. The dashed profiles are in the outer ring of the CLV within a radius of 60–120 km.

4.4. Long-Term Trend Change

Generally, an ACE will leave footprints of a warm anomaly in the SST fields. However, due to strong vertical mixing, the LV produces a cold anomaly in the SST fields. The temperature anomaly (SSTA) and the vorticity are mainly displayed in the LV central area. However, the negative vorticity is surrounded by positive vorticity. Thus, the spatial averaged value of the vorticity is more affected by the LV peripheral area. The vorticity, KE, and SSHD are sensitive to the daily LV boundary. Satellite data for the SST have the advantages of a high resolution and longer time records. We used daily SST data to analyze the long-term time series of surface features of the LV.

The original time series is the spatially averaged SST over the CLV sea area. The SST time series is in the range of 4 °C–11 °C throughout the year and has significant seasonal variation (Figure 8a). It also has a long-term increasing trend. The SSH has a similar variation to the SST (not shown). The CLV's surface temperature shows an independent cold imprint compared with the background (Figure 8b). The surface temperature of the CLV's core is lower than 6.8 °C. The background temperature gradually decreases from 7.2 °C in the southeast to 6.4 °C in the northwest. The southeast sea area is more affected by the NwASC.

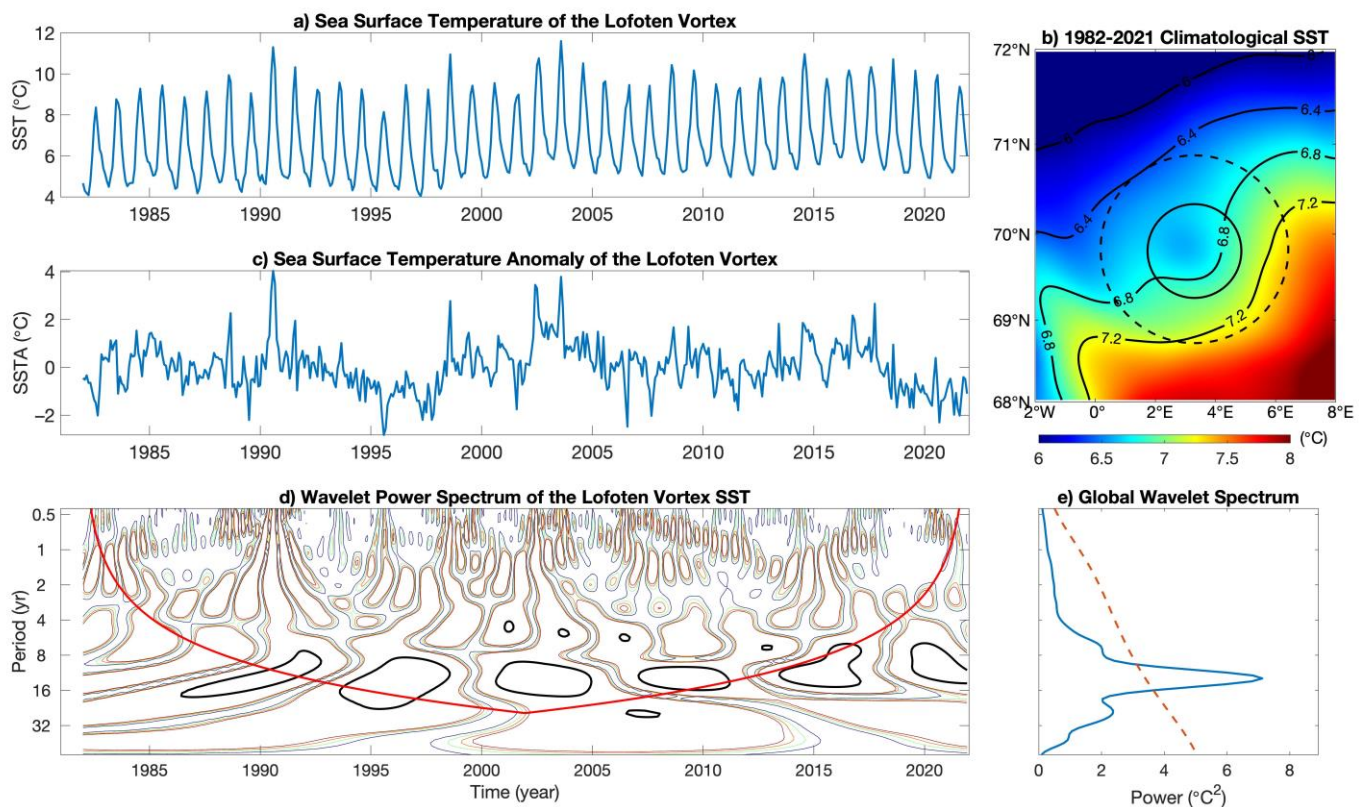


Figure 8. Wavelet analysis of the time series of the spatially averaged SST throughout the CCLV sea area. (a) Original SST time series. (b) Spatial field of the climatological SST from 1982 to 2021. (c) Residual SST time series (with trend and annual cycle removed). (d) Wavelet power spectrum of the residual SST time series. Statistical significance ($p = 0.05$, Student's t test) is shown by thick red isolines. (e) Global wavelet spectrum and the red noise line.

The residual SST time series was obtained by removing the trend and seasonal cycle from the original SST time series (Figure 8c). Wavelet analysis was performed for the residual SST time series. We used the “DOG” wavelet as the wavelet basis function. The highest energy intensity is shown by black isolines. The wavelet power spectrum shows that the time series of the SST covers a significant period of 8–16 years (Figure 8d). The global wavelet spectrum shows that the result passes the red noise test (Figure 8e).

To better display and analyze the SST variations in the LV, we removed only the seasonal cycle from the daily SST time series (Figure 9a). The 24-month moving average SST time series shows periodic fluctuations in an increasing trend. This trend shows increases of approximately $1.5\text{ °C}/40$ years throughout a period from 1982 to 2021. Although limited by the length of the time series, the wavelet analysis still shows that the SST covers a significant period of 8–16 years. In the low-frequency range, we can divide the periods into 1982–1997, 1998–2011, and 2012–2021. The stages of increasing warming include 1982–1991, 1998–2003, and 2012–2017. The stages of decrease toward cooling include 1992–1997, 2004–2011, and 2018–2021. The first stage, 1982–1991, is one of inclination toward warming, but the temperature value is at the lowest point in the trending line. To avoid the inefficient effect of periodic averaging, we divided the periods into new stages depending on whether they were above or below the trending line.

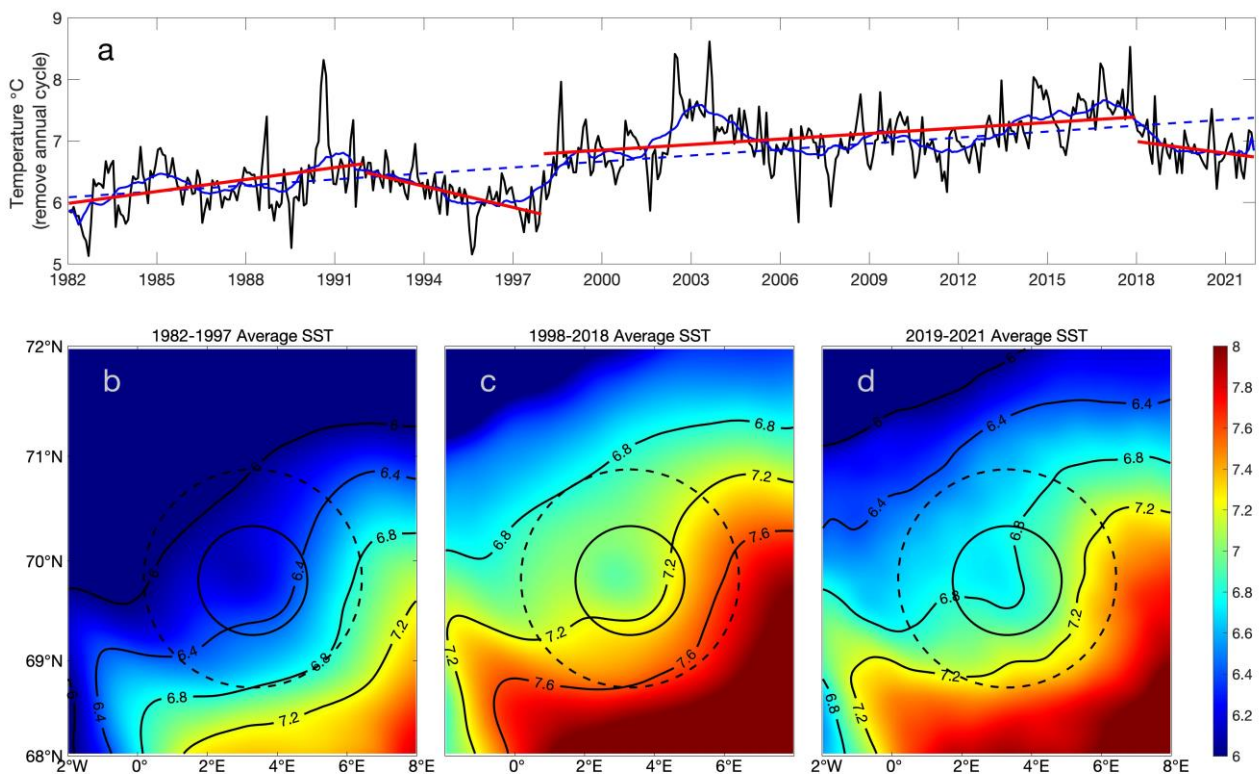


Figure 9. Trend and variations in the SST throughout the CLV sea area. (a) Removed annual cycle SST series (the black thick line) and 24-month moving average SST time series (the blue line). A long trend throughout the period of 01-01-1982 to 31-12-2021 (black dashed line) and significantly segmental trends (red lines) can be seen. Spatially averaged SST can be seen throughout the periods of (b) 1982–1997, (c) 1998–2018, and (d) 2019–2021.

The spatially averaged SST fields throughout the periods of 1992–1997, 1998–2017, and 2018–2021 are presented in Figure 9b–d. Meanwhile, the background temperature fields display the local trends. From southeast to northwest, the temperature decreases from 6.8 °C to 6 °C, from 7.6 °C to 6.8 °C, and from 7.2 °C to 6.4 °C. The surface temperature of the CLV’s core is isolated from the background and presents as a “cool” anomaly. Here, we are more concerned with the vertical mixing that causes the surface cool anomaly in the LV. Thus, we sought to determine whether stronger vertical mixing signals exist in the decreasing stage of the surface temperature.

The available Argo profile data start from 2002, and the surface temperature of the LV has shown a “cold” signal since 2018. Accordingly, we divided the Argo profile data for the CLV sea area into two periods. The first is the period of 2002–2017, and the second is the period of 2018–2021. The monthly mean Argo profiles for these two periods are presented in Figure 10. The climatological monthly salinity, potential temperature, and potential density profiles are averaged within the inner circle of the CLV, with a radius of 60 km. All the profiles show a deeper vertical mixing in the second period after 2018. This stronger mixing causes the salinity and temperature to increase and the density to decrease at the core depth of the LV. In the upper ocean, the salinity of the LV decreases by 0.1 PSU. This large salinity difference in the upper ocean indicates that the salinity of the North Atlantic Warm Current is decreasing. The temperature of the LV in the upper ocean is decreased. These results are consistent with the surface temperature fields. The salinity and temperature have opposite contributions to the density. Under the combined effects of salinity and temperature, the density change in the upper layer of the LV is not clear, but the density decreases significantly at the core depth.

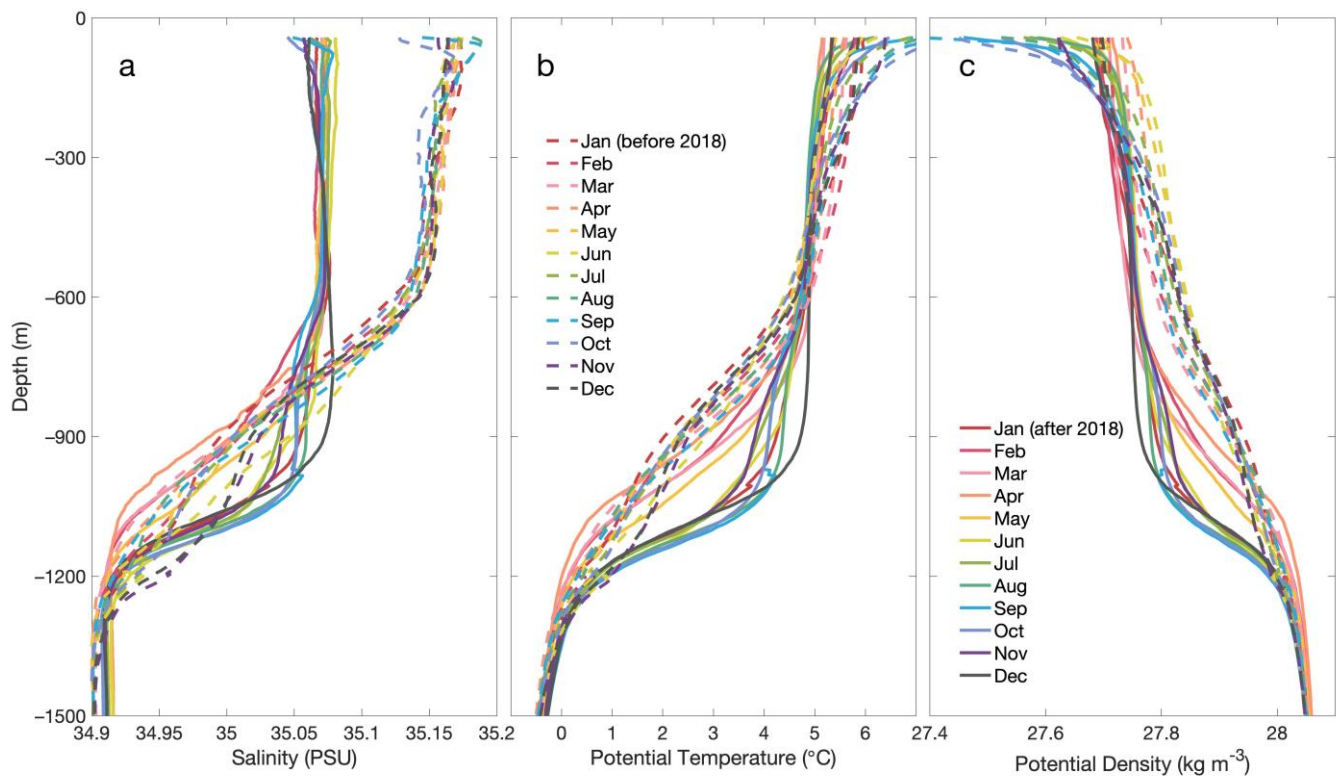


Figure 10. Climatological monthly (a) salinity, (b) potential temperature, and (c) potential density profiles in the inner circle of the CLV within a radius of 60 km. The dashed profiles are the mean profiles throughout the period of 2002–2017, and the solid lines are the mean profiles since 2018.

5. Discussions and Conclusions

Our results indicate the seasonal and long-term variations in the surface and vertical structures of the LV. This analysis of the LV, as a strong ACE, contributes to our understanding of vertical mixing in the LB.

The basic surface physical characteristics of the LV were obtained using drifter data and satellite altimeter data. The CLV, with a radius of 60 km, is centered at 69.8°N and 3.3°E . The climatological surface height difference induced by the LV can reach 12 cm, and the derived outer tangential velocity is approximately 30 cm/s. The kinetic energy of the CLV is approximately $300\text{ cm}^2\text{ s}^{-2}$. Within the positive vorticity zone, the vorticity of the CLV core is approximately -10^{-5} s^{-1} . Nearly all the physical parameters show that the LV is a strong ACE. More importantly, the seasonal analysis of the sea surface characteristics demonstrates that the LV is relatively stable in terms of its spatial position but has significant seasonal variations.

Eddies are often tiled along the vertical direction due to their propagation [42]. However, the LV is a quasi-stationary ACE. The vertical structure of the LV is relatively stable and nontiled. Given the temperature and salinity data of the Argo profiles are sorted by the radius range, the vertical characteristics of the LV were explored in terms of the spatial distribution and monthly variations. At the depth of 20 m to 1500 m, the salinity within the LV (0–60 km) decreases from 35.1 PSU to 34.9 PSU, the potential temperature decreases from 6°C to -0.5°C , and the potential density increases from 27.6 kg m^{-3} to 28.05 kg m^{-3} . The vertical mixing characteristic is significant in the center zone, and the high-mixing depth of the climatological temperature and salinity profiles can reach 1000 m. Compared with the surrounding waters, the LV is colder and fresher in the upper layer, while it warmer and saltier at the core depth of 500–1300 m. This is a typical anomaly structure for an ACE in the LB. Due to high mixing, the temperature of the ACEs is slightly colder than that inside the CEs in the upper layer [13]. At a depth of 900 m, the salinity anomaly of the LV is $\Delta S = 0.2\text{ PSU}$, the potential temperature anomaly is $\Delta T = 5.5^{\circ}\text{C}$, and the potential density

anomaly is $\Delta\rho = -0.25 \text{ kg m}^{-3}$. Limited by the available records of Argo data, a more detailed analysis of the three-dimensional structure of the LV, especially the evolution of its three-dimensional structure, still needs to be carried out using high-resolution numerical model results.

The LV has significant seasonal variations in the spatial fields. The surface height difference throughout the LV area is higher in May and lower in September. Hence, various physical parameters related to the SSHD also reach their maximum extreme value in May and their minimum value in September. For example, the kinetic energy of the LV is higher than $300 \text{ cm}^2 \text{ s}^{-2}$ in May but is only around $200 \text{ cm}^2 \text{ s}^{-2}$ in Sep. The negative vorticity of the LV core reaches -10^{-5} s^{-1} and is shielded by a strong positive vorticity of 10^{-5} s^{-1} in May. The climatological results of the sea surface fields show that the vortex is strongest in spring, which differs from the previous study results showing that the LV is intensified in winter through convection.

The climatological monthly variation in the vertical structure was also investigated using Argo profiles. In the upper 400 m, the sea water temperature within the LV starts to warm up in May, reaches the highest value in September and October, and then cools from November until it reaches its lowest value in April. It is cooler than the background water throughout the whole year due to vertical mixing. At the LV core depth of 600–1200 m, due to vertical mixing, the vertical penetration of the temperature and salinity inside the LV reaches deeper than that of the outside background water. Nevertheless, being limited to the available profiles, with an uneven distribution throughout the LV, the monthly vertical profiles for the core depth of the LV do not present the anticipated variations.

To avoid the influences of the central movement and peripheral deformation of the LV, we used daily SST data (rather than KE, SSHD, and other parameters) to analyze the long-term variation in the LV. The surface temperature of the CLV's core is approximately $6.8 \text{ }^\circ\text{C}$. The averaged SST time series across the CLV varies from $4 \text{ }^\circ\text{C}$ to $11 \text{ }^\circ\text{C}$. After removing the seasonal cycle and the increasing trend, the wavelet analysis of the time series of the SST anomaly (SSTA) shows that the SSTA through the LV shows a period of variation of 8–16 years. This periodic variation in the SSTA implies variations in the strength of vertical mixing. The decreasing (or increasing) SSTA can be explained by strengthened (or weakened) vertical mixing. This strengthened vertical mixing will induce cooling and freshening in the upper layer of the LV and warming and salinization at the core depth of the LV.

Since 2018, the vertical mixing has been in a stage of strengthening, accompanied by decreasing SSTA. If the SSTA has an internal variation, similar to that observed in the year 1998, the SSTA will dramatically increase in the next stage. In the meantime, against the background of the increasing temperature and decreasing salinity of the North Atlantic, the degree of vertical mixing will dramatically decrease throughout the LV and in the LB.

The LV is a quasi-permanent eddy with relatively stable spatial variations. In its seasonal variation, the strengthening of the LV can be attributed to eddy merging and winter convection. Additionally, high-frequency variations in the LV's strength may be affected by eddies shed from the NwASC. To better understand these processes, further analysis of eddy tracking and merging is needed. Using 30-year SST satellite data and the available Argo profile data, we established a relationship between SSTA and vertical mixing. In terms of its long-term variations, SSTA can serve as an indicator of the LV's vertical mixing variations. The LB is one of the major areas of deep vertical mixing in the Nordic Seas. As a potential indicator of the LB, the vertical mixing of the LV may be a reflection of the strengthening of, and periodic variations in, the NADW. However, a longer time series is required to fully explore the relationship between them.

Author Contributions: Conceptualization, Y.L. and J.W.; methodology, Y.L. and J.M.; software, Y.L. and G.H.; validation, Y.L., J.W., and G.H.; formal analysis, Y.L. and X.L.; investigation, Y.L.; resources, Y.L. and Q.J.; data curation, Y.L. and G.H.; writing—original draft preparation, Y.L. and J.M.; writing—review and editing, Y.L. and G.H.; visualization, Y.L. and J.C.; supervision, X.L. and Q.J.; project

administration, Y.L. and J.C.; funding acquisition, Y.L. and G.H. All authors have read and agreed to the published version of the manuscript.

Funding: This study was supported by the National Key Research and Development Program of China (2018YFA0605904); the Southern Marine Science and Engineering Guangdong Laboratory (Zhuhai) (SML2020SP007); the Innovation Group Project of Southern Marine Science and Engineering Guangdong Laboratory (Zhuhai) (311020004); and the Natural Science Foundation of China Project (42206005, 41806030 and 41806004).

Data Availability Statement: The drifter data were obtained from the Global Drifter Program (<https://www.aoml.noaa.gov/phod/gdp/index.php> accessed on 15 September 2022). The SSH and SST data we used were obtained from the Copernicus Marine Environment Monitoring Service (<http://marine.copernicus.eu/> accessed on 22 September 2022). The temperature and salinity profile data were obtained from the Argo buoy observations (<ftp://ftp.ifremer.fr/ifremer/argo/geo> accessed on 25 September 2022).

Acknowledgments: We thank the editor, the academic editor, and anonymous reviewers for their constructive comments and helpful suggestions on the earlier version of the manuscript.

Conflicts of Interest: The authors declare no conflict of interest.

References

- Blindheim, J.; Rey, F. Water-mass formation and distribution in the nordic seas during the 1990s. *ICES J. Mar. Sci.* **2004**, *61*, 846–863. [[CrossRef](#)]
- Boyer, T.P.; Levitus, S.; Antonov, J.; Locarnini, R.; Garcia, H. Linear trends in salinity for the world ocean, 1955–1998. *Geophys. Res. Lett.* **2005**, *32*, L01604. [[CrossRef](#)]
- Nilsen, J.E.Ø.; Nilsen, F. The atlantic water flow along the vøring plateau: Detecting frontal structures in oceanic station time series. *Deep-Sea Res. Part I* **2007**, *54*, 297–319. [[CrossRef](#)]
- Bosse, A.; Fer, I.; Lilly, J.M.; Søiland, H. Dynamical controls on the longevity of a non-linear vortex: The case of the lofoten basin eddy. *Sci. Rep.* **2019**, *9*, 13448. [[CrossRef](#)]
- Spall, M.A.; Almansi, M.; Huang, J.; Haine, T.W.; Pickart, R.S. Lateral redistribution of heat and salt in the nordic seas. *Progr. Oceanogr.* **2021**, *196*, 102609. [[CrossRef](#)]
- Segtnan, O.; Furevik, T.; Jenkins, A. Heat and freshwater budgets of the nordic seas computed from atmospheric reanalysis and ocean observations. *J. Geophys. Res. Ocean.* **2011**, *116*, C11003. [[CrossRef](#)]
- Mayot, N.; Matrai, P.; Arjona, A.; Bélanger, S.; Marchese, C.; Jaegler, T.; Ardyna, M.; Steele, M. Springtime export of arctic sea ice influences phytoplankton production in the greenland sea. *J. Geophys. Res. Ocean.* **2020**, *125*, e2019JC015799. [[CrossRef](#)]
- Rossby, T.; Prater, M.; Søiland, H. Pathways of inflow and dispersion of warm waters in the nordic seas. *J. Geophys. Res. Ocean.* **2009**, *114*, C04011. [[CrossRef](#)]
- Björk, G.; Gustafsson, B.G.; Stigebrandt, A. Upper layer circulation of the nordic seas as inferred from the spatial distribution of heat and freshwater content and potential energy. *Polar. Res.* **2001**, *20*, 161–168. [[CrossRef](#)]
- Nilsen, J.E.Ø.; Falck, E. Variations of mixed layer properties in the norwegian sea for the period 1948–1999. *Progr. Oceanogr.* **2006**, *70*, 58–90. [[CrossRef](#)]
- Richards, C.G.; Straneo, F. Observations of water mass transformation and eddies in the lofoten basin of the nordic seas. *J. Phys. Oceanogr.* **2015**, *45*, 1735–1756. [[CrossRef](#)]
- Volkov, D.L.; Belonenko, T.V.; Foux, V.R. Puzzling over the dynamics of the lofoten basin—a sub-arctic hot spot of ocean variability. *Geophys. Res. Lett.* **2013**, *40*, 738–743. [[CrossRef](#)]
- Raj, R.P.; Johannessen, J.A.; Eldevik, T.; Nilsen, J.E.Ø.; Halo, I. Quantifying mesoscale eddies in the Lofoten Basin. *J. Geophys. Res. Ocean.* **2016**, *121*, 4503–4521. [[CrossRef](#)]
- Gordeeva, S.; Zinchenko, V.; Koldunov, A.; Raj, R.P.; Belonenko, T. Statistical analysis of long-lived mesoscale eddies in the lofoten basin from satellite altimetry. *Adv. Space Res.* **2021**, *68*, 364–377. [[CrossRef](#)]
- Ikeda, M.; Johannessen, J.; Lygre, K.; Sandven, S. A process study of mesoscale meanders and eddies in the norwegian coastal current. *J. Phys. Oceanogr.* **1989**, *19*, 20–35. [[CrossRef](#)]
- Johannessen, J.A.; Sandven, S.; Lygre, K.; Svendsen, E.; Johannessen, O. Three-dimensional structure of mesoscale eddies in the norwegian coastal current. *J. Phys. Oceanogr.* **1989**, *19*, 3–19. [[CrossRef](#)]
- Köhl, A. Generation and stability of a quasi-permanent vortex in the lofoten basin. *J. Phys. Oceanogr.* **2007**, *37*, 2637–2651. [[CrossRef](#)]
- Rossby, T.; Ozhigin, V.; Ivshin, V.; Bacon, S. An isopycnal view of the nordic seas hydrography with focus on properties of the lofoten basin. *Deep-Sea Res. Part I* **2009**, *56*, 1955–1971. [[CrossRef](#)]
- Sandalyuk, N.V.; Bosse, A.; Belonenko, T.V. The 3-d structure of mesoscale eddies in the lofoten basin of the norwegian sea: A composite analysis from altimetry and in situ data. *J. Geophys. Res. Oceans.* **2020**, *125*, e2020JC016331. [[CrossRef](#)]

20. Furevik, T.; Mauritzen, C.; Ingvaldsen, R. The flow of Atlantic water to the Nordic Seas and Arctic Ocean. In *Arctic Alpine Ecosystems and People in a Changing Environment*; Ørbæk, J.B., Kallenborn, R., Tombre, I., Hegseth, E.N., Falk-Petersen, S., Hoel, A.H., Eds.; Springer: Berlin, Germany, 2007; pp. 123–146.
21. Andersson, M.; Orvik, K.; LaCasce, J.; Koszalka, I.; Mauritzen, C. Variability of the norwegian atlantic current and associated eddy field from surface drifters. *J. Geophys. Res. Ocean.* **2011**, *116*, C08032. [[CrossRef](#)]
22. Chafik, L.; Nilsson, J.; Skagseth, Ø.; Lundberg, P. On the flow of a atlantic water and temperature anomalies in the nordic seas toward the arctic ocean. *J. Geophys. Res. Ocean.* **2015**, *120*, 7897–7918. [[CrossRef](#)]
23. Alexeev, G.; Bagryantsev, M.; Bogorodsky, P.; Vasin, V.; Shirokov, P. Structure and circulation of water masses in the area of an anticyclonic vortex in the north-eastern part of the norwegian sea. *Russ. Probl. Arct. Antarct.* **1991**, *65*, 14–23.
24. Ivanov, Y.; Korablev, A. Formation and regeneration of the pycnocline lens in the norwegian sea. *Russ. Meteorol. Hydrol.* **1995**, *9*, 62–69.
25. Ivanov, Y.; Korablev, A. Dynamics of an intrapycnocline lens in the Norwegian sea. *Russ. Meteorol. Hydrol.* **1995**, *10*, 32–37.
26. Pereskokov, A. On the physical nature of large-scale counter-cyclical cycle in the water column of the norwegian sea. *Rep. Acad. Sci.* **1999**, *364*, 549–552.
27. Bashmachnikov, I.; Sokolovskiy, M.; Belonenko, T.; Volkov, D.; Isachsen, P.; Carton, X. On the vertical structure and stability of the lofoten vortex in the norwegian sea. *Deep-Sea Res. Part I* **2017**, *128*, 1–27. [[CrossRef](#)]
28. Romantcev, V. Large-scale structure and characteristics of the average circulation of the water. *Probl. Arctic. Antarc.* **1991**, *65*, 75–97.
29. Søiland, H.; Prater, M.; Rossby, T. Rigid topographic control of currents in the nordic seas. *Geophys. Res. Lett.* **2008**, *35*, L18607. [[CrossRef](#)]
30. Koszalka, I.; LaCasce, J.; Andersson, M.; Orvik, K.; Mauritzen, C. Surface circulation in the nordic seas from clustered drifters. *Deep-Sea Res. Part I* **2011**, *58*, 468–485. [[CrossRef](#)]
31. Søiland, H.; Chafik, L.; Rossby, T. On the long-term stability of the lofoten basin eddy. *J. Geophys. Res. Ocean.* **2016**, *121*, 4438–4449. [[CrossRef](#)]
32. Trodahl, M.; Isachsen, P.E.; Lilly, J.M.; Nilsson, J.; Kristensen, N.M. The regeneration of the lofoten vortex through vertical alignment. *J. Phys. Oceanogr.* **2020**, *50*, 2689–2711. [[CrossRef](#)]
33. Volkov, D.L.; Kubryakov, A.A.; Lumpkin, R. Formation and variability of the lofoten basin vortex in a high-resolution ocean model. *Deep-Sea Res. Part I* **2015**, *105*, 142–157. [[CrossRef](#)]
34. Belkin, I.; Foppert, A.; Rossby, T.; Fontana, S.; Kincaid, C. A double-thermostad warm-core ring of the gulf stream. *J. Phys. Oceanogr.* **2020**, *50*, 489–507. [[CrossRef](#)]
35. Dong, C.; Liu, Y.; Lumpkin, R.; Lankhorst, M.; Chen, D.; McWilliams, J.C.; Guan, Y. A scheme to identify loops from trajectories of oceanic surface drifters: An application in the Kuroshio Extension region. *J. Atmos. Ocean. Technol.* **2011**, *28*, 1167–1176. [[CrossRef](#)]
36. Wright, D.G.; Pawlowicz, R.; McDougall, T.J.; Feistel, R.; Marion, G.M. Absolute Salinity, “Density Salinity” and the Reference-Composition Salinity Scale: Present and future use in the seawater standard TEOS-10. *Ocean. Sci.* **2011**, *7*, 1–26. [[CrossRef](#)]
37. Torrence, C.; Compo, G. A practical guide to wavelet analysis. *Bull. Am. Meteorol. Soc.* **1998**, *79*, 61–78. [[CrossRef](#)]
38. Silva, C.B.; Silva, M.E.S.; Krusche, N.; Ambrizzi, T.; de Jesus Ferreira, N.; da Silva Dias, P.L. The analysis of global surface temperature wavelets from 1884 to 2014. *Theor. Appl. Climatol.* **2019**, *136*, 1435–1451. [[CrossRef](#)]
39. Raj, R.P.; Chafik, L.; Nilsen, J.E.Ø.; Eldevik, T.; Halo, I. The lofoten vortex of the nordic seas. *Deep-Sea Res. Part I* **2015**, *96*, 1–14. [[CrossRef](#)]
40. Orvik, K.A. The deepening of the Atlantic water in the Lofoten Basin of the Norwegian Sea, demonstrated by using an active reduced gravity model. *Geophys. Res. Lett.* **2004**, *31*, L01306. [[CrossRef](#)]
41. Dickson, R.R.; Brown, J. The production of north atlantic deep water: Sources, rates, and pathways. *J. Geophys. Res. Ocean.* **1994**, *99*, 12319–12341. [[CrossRef](#)]
42. Li, H.; Xu, F.; Wang, G. Global mapping of mesoscale eddy vertical tilt. *J. Geophys. Res. Ocean.* **2022**, *127*, e2022JC019131. [[CrossRef](#)]

Disclaimer/Publisher’s Note: The statements, opinions and data contained in all publications are solely those of the individual author(s) and contributor(s) and not of MDPI and/or the editor(s). MDPI and/or the editor(s) disclaim responsibility for any injury to people or property resulting from any ideas, methods, instructions or products referred to in the content.